3D finite-difference frequency-domain modeling of controlled-source electromagnetic data: Direct solution and optimization for high accuracy

Rita Streich[1]

ABSTRACT

Three-dimensional modeling of marine controlled-source electromagnetic (CSEM) data is vital to improve the understanding of electromagnetic (EM) responses collected in increasingly complex geologic settings. A modeling tool for simulating 3D marine CSEM surveys, based on a finite-difference discretization of the Helmholtz equation for the electric fields, has been developed. Optimizations for CSEM simulations include the use of a frequency-domain technique, a staggering scheme that reduces inaccuracies especially for horizontal electric-dipole sources located near the seafloor, and a new interpolation technique that provides highly accurate EM field values for receivers located in the immediate vicinity of the seafloor. Source singularities are eliminated through a secondary-field approach, in which the primary fields are computed analytically for a homogeneous or a 1D layered background; the secondary fields are computed using the finite-difference technique. Exploiting recent advances in computer technology and algorithmic developments, the system of finite-difference equations is solved using the MUMPS direct-matrix solver. In combination with the other optimizations, this allows accurate EM field computations for moderately sized models on small computer clusters. The explicit availability of matrix factorizations is advantageous for multisource modeling and makes the algorithm well suited for future use within an inversion scheme. Comparisons of simulated data for (1) 1D models to data generated using a 1D reflectivity technique and (2) 3D models to published 3D data demonstrate the accuracy and benefits of the approach.

INTRODUCTION

Marine controlled-source electromagnetic (CSEM) surveying techniques are of increasing importance for hydrocarbon explora-

tion (Johansen et al., 2005). Three-dimensional modeling studies are vital to understanding electromagnetic (EM) responses of hydrocarbon reservoirs and facilitate faithful interpretation of data acquired in complex geologic settings.

Various approaches exist for 3D EM modeling. An overview is provided, for example, by Avdeev (2005). Common approaches include finite-element techniques (Badea et al., 2001; Mitsuhata and Uchida, 2004; Schwarzbach and Spitzer, 2006), finite-difference (Newman and Alumbaugh, 1995; Alumbaugh et al., 1996; Champagne II et al., 2001; Weiss and Newman, 2002) and closely related finite-volume methods (Mackie et al., 1993; Haber et al., 2000; Haber and Ascher, 2001; Weiss and Constable, 2006), and integral-equation techniques (Wannamaker, 1991; Avdeev et al., 2002). In addition to these frequency-domain approaches, new efficient time-domain methods are emerging (Oldenburg et al., 2007; Afanasjew et al., 2008; Börner et al., 2008), and finite-difference time-domain techniques are being developed further (Commer and Newman, 2004; Maaø, 2007). Finite-difference methods are probably simplest in concept, but finite-element techniques are most flexible in accounting for model geometry (Avdeev, 2005); however, they are not as straightforward to implement as FD methods. Integral-equation methods can be highly efficient for relatively simple models, but their computational complexity increases with increasing model complexity (Mackie et al., 1993).

Most modeling approaches result in a system of equations that can be written as $\mathbf{MF} = \mathbf{J}$, where $\mathbf{M}$ is a system matrix, $\mathbf{F}$ is a representation of the unknown EM fields (in terms of electric or magnetic fields or potentials), and $\mathbf{J}$ represents a source-current density. To solve this system for $\mathbf{F}$, iterative and direct solvers are available.

Iterative solvers (Woźniakowski, 1980; Freund and Nachtigal, 1994) are used within most current 3D EM modeling approaches (e.g., Newman and Alumbaugh, 1995; Haber and Ascher, 2001; Weiss and Constable, 2006). They need relatively little memory compared to direct solvers because they require storing only matrix-vector products. Iterative solvers also require less computation time than direct ones if only a single field solution is to be computed. However, iterative solvers are expensive for the multisource prob-

lems typical of CSEM surveying (Oldenburg et al., 2008), and ill-conditioning of matrices can lead to poor iterative results.

Direct-solution techniques are less prone to ill-conditioning, provided that sufficient numerical precision is used. The principle of direct solution, comprising a single expensive matrix factorization followed by inexpensive solutions for many right-hand sides, lends itself to multisource problems. Unfortunately, for 3D models, the factorization step can entail tremendous cost in terms of memory and computation time. This has previously inhibited the use of direct solvers for 3D modeling, although they have been applied for 2D problems (e.g., Ravaut et al., 2004). Given the increasing availability and power of computer clusters as well as the gradual improvement of direct-solution algorithms (Amestoy et al., 2001, 2006; Schenk and Gärtner, 2004, 2006), direct solvers are being reconsidered for 3D problems of limited, yet previously intractable sizes (Operto et al., 2007; Börner et al., 2008; Oldenburg et al., 2008; Blome et al., 2009).

Because of the inherent limitation of model sizes posed by direct solvers, their application to 3D problems must be accompanied by optimizations of the modeling scheme in the quest for achieving acceptable accuracy using relatively coarse grids. In CSEM modeling, particular challenges exist that require well-adapted strategies to keep the grid size manageable. First, to avoid having to sample the model very densely near the source singularity, we can use secondary-field approaches that exclude source singularities from discrete numerical calculations (Newman and Alumbaugh, 1995). To make a secondary-field approach effective, the background should be chosen such that secondary sources do not arise in close proximity to the primary source. Second, it is desirable to include air in CSEM models because in many marine CSEM applications, a significant part of the EM fields propagates through the air. The substantial material contrast between air and the subsurface, and the undamped wavefield propagation in air must be handled appropriately while adhering to limited grid sizes. Third, CSEM receivers typically are located at the seafloor, which implies that EM field values must be extracted in the immediate vicinity of field discontinuities. To facilitate extracting field values closer than a cell's distance from model interfaces, appropriate interpolation strategies are required.

I implement a code for modeling CSEM surveys that addresses these challenges. A finite-difference frequency-domain (FDFD) approach is used because the frequency-domain approach corresponds well to the CSEM survey practice of extracting only a few discrete frequencies from the data and because of the relative simplicity of the FDFD method. The MUMPS direct-matrix solver (Amestoy et al., 2006) solves the system of finite-difference equations. A staggering scheme used is advantageous for near-seafloor horizontal-dipole sources, and a secondary-field approach with 1D background models facilitates accurate simulations for sources near the seafloor and air present in the model. In addition, a new interpolation scheme extracts correct EM field values in the immediate vicinity of field discontinuities.

I first describe the modeling scheme and the specific optimizations for modeling CSEM surveys. Computational aspects of the memory and time requirements for the direct-solution approach are addressed briefly. Then the accuracy of the chosen approach is verified and the advantages of the specific optimizations are demonstrated by comparing 3D FDFD modeling results with reference results obtained from an analytic 1D reflectivity method (Løseth and Ursin, 2007). Finally, I present a 3D modeling example and verify the results against published data.

MODELING APPROACH

A finite-difference approach is used to solve Maxwell's equations in the frequency domain. Maxwell's equations can be written as

$$\nabla \times \mathbf{E} + j\omega\mu_0\mathbf{H} = -\mathbf{K}, \quad (1a)$$

$$\nabla \times \mathbf{H} - \sigma^*\mathbf{E} = \mathbf{J}, \quad (1b)$$

where $\mathbf{E}$ and $\mathbf{H}$ are the electric and magnetic fields, $\mathbf{J}$ and $\mathbf{K}$ are electric and magnetic sources, ω is the angular frequency, μ_0 is the vacuum magnetic permeability (permeability variations are not considered), and the medium parameter $\sigma^* = \sigma + j\omega\varepsilon$ contains the electric conductivity σ and permittivity $\varepsilon = \varepsilon_r\varepsilon_0$, where ε_0 is the vacuum dielectric permittivity and ε_r is the relative permittivity of the medium. To exclude source-point singularities from the numerical computations, the fields are split into a primary part and a secondary part (Newman and Alumbaugh, 1995). The physical sources are included in the Maxwell equations for the primary fields, which can be evaluated analytically. The secondary fields are computed by the FDFD method. The equations for the secondary (or scattered) fields then become

$$\nabla \times \mathbf{E}^S + j\omega\mu_0\mathbf{H}^S = 0, \quad (2a)$$

$$\nabla \times \mathbf{H}^S - \sigma^*\mathbf{E}^S = (\sigma^* - \sigma^{P*})\mathbf{E}^P, \quad (2b)$$

where superscripts P and S denote the primary and secondary fields, respectively, and the term $(\sigma^* - \sigma^{P*})\mathbf{E}^P$ is identified as a secondary-source term. By taking the curl of equation 2a and substituting equation 2b, a vector Helmholtz equation for the secondary electric field is obtained:

$$\nabla \times \nabla \times \mathbf{E}^S + j\omega\mu_0\sigma^*\mathbf{E}^S = -j\omega\mu_0(\sigma^* - \sigma^{P*})\mathbf{E}^P. \quad (3)$$

Equation 3 forms the basis of the presented modeling scheme; it is well suited for simulations in typical CSEM frequency ranges of ~ 0.1 to -10 Hz. Toward the static limit ($\omega \to 0$), the terms containing information on the medium properties tend to zero, making the solution nonunique (e.g., Smith, 1996b). Consequently, at very low frequencies, alternative formulations must be used.

Sources

Electric-dipole sources and magnetic-loop sources with general orientations are considered. Electric sources $\mathbf{J} = (J_x, J_y, J_z)$ are characterized by the source current $I(\omega)$ and the dipole orientation and length $\mathbf{l} = (l_x, l_y, l_z)$ as (Løseth and Ursin, 2007)

$$\mathbf{J} = I(\omega)\mathbf{l}\delta(\mathbf{x} - \mathbf{x_s}), \quad (4)$$

where $\mathbf{x}_s = (x_s, y_s, z_s)$ is the source position. Similarly, magnetic-loop sources $\mathbf{K} = (K_x, K_y, K_z)$ are described by

$$\mathbf{K} = -j\omega\mu_0 I(\omega)\mathbf{a}\delta(\mathbf{x} - \mathbf{x_s}), \quad (5)$$

where $\mathbf{a} = (a_x, a_y, a_z)$ are the areas of the current-carrying loop projected into the (y,z), (x,z), and (x,y) planes, respectively. To obtain more general sources (e.g., for simulating a known radiation pattern), combinations of elementary sources described in equations 4 and 5 can be used.

Background models for primary fields

The primary fields are computed for a homogeneous background model having the conductivity and permittivity given at the source point or for a 1D horizontally layered model. For the homogeneous background model, explicit expressions for the EM fields in the frequency domain can be derived (van der Kruk [2001]; see also de Hoop [1995] and van der Kruk et al. [2003]).

For 1D layered media, analytic expressions for the EM fields can be found in the horizontal wavenumber-frequency domain (e.g., Ursin, 1983; Løseth and Ursin, 2007). Space-domain fields are obtained by rewriting the inverse spatial Fourier transforms of these expressions in cylindrical coordinates and numerically evaluating the resulting Bessel function integrals. The analytic 1D solution I use is an isotropic version of the one given in Løseth and Ursin (2007). To obtain accurate integral values, I apply the continued fractions method described in Chave (1983) in conjunction with highly accurate asymptotic formulas for the Bessel functions given in Hart et al. (1968).

Finite-difference discretization

To obtain a finite-difference solution, the Helmholtz equation 3 is discretized on a staggered grid. From the main grid nodes (i,j,k) located in the cell centers, the electric-field components E_x, E_y, and E_z are offset by a half-cell in the x-, y-, and z-directions, respectively (Figure 1). The magnetic-field component H_x is staggered in y and z, H_y in x and z, and H_z in x and y. The discrete finite-difference equations are given in Appendix A.

Model conductivity and permittivity are assumed to be constant within each cell. Because the electric-field components are located at positions where the medium properties could be discontinuous, medium averaging is required. I obtain staggered model properties by harmonic averaging (Smith, 1996a; Haber et al., 2000; Haber and Ascher, 2001). For example, the x-staggered complex conductivity is

$$\sigma^*_{i+\frac{1}{2},j,k} = \Delta x_{i+\frac{1}{2}} \left(\frac{\Delta x_i}{2\sigma^*_{i,j,k}} + \frac{\Delta x_{i+1}}{2\sigma^*_{i+1,j,k}} \right)^{-1}, \quad (6)$$

where Δx_i and Δx_{i+1} are the widths of the main grid cells i and $i+1$ and $\Delta x_{i+\frac{1}{2}}$ is the width of the staggered grid cell that extends between the centers of cells i and $i+1$. The harmonic averaging en-
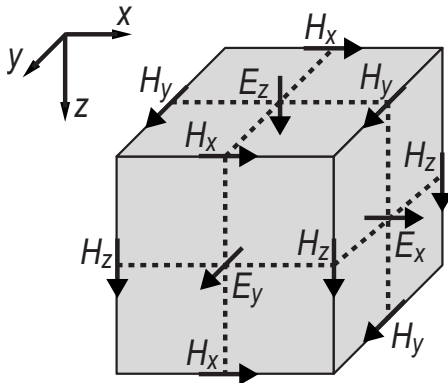

Figure 1. The coordinate system and staggering scheme used. Electric-field components E_x, E_y, and E_z are located on the cell faces; magnetic field components H_x, H_y, and H_z are on the edges.

sures the equality of the current densities derived from nonaveraged and averaged conductivities across cell boundaries, i.e., it enforces

$$\sigma^*_{i,j,k} E^x_{i,j,k} = \sigma^*_{i+1,j,k} E^x_{i+1,j,k}$$

$$= \sigma^*_{i+\frac{1}{2},j,k} \frac{\Delta x_i E^x_{i,j,k} + \Delta x_{i+1} E^x_{i+1,j,k}}{\Delta x_i + \Delta x_{i+1}}. \quad (7)$$

The discrete equations (see Appendix A) are assembled into a system of equations

$$\mathbf{M}\mathbf{E}^S = \mathbf{J}^S, \quad (8)$$

where $\mathbf{M}$ is the system matrix of dimension $(3N_x \times N_y \times N_z)^2$ for a model with $N_x \times N_y \times N_z$ cells; vector $\mathbf{E}^S$ of length $3N_x \times N_y \times N_z$ contains the secondary electric field values E^S_x, E^S_y, E^S_z for all nodes; and $\mathbf{J}^S$ (length $3N_x \times N_y \times N_z$) is the secondary-source vector given by the right-hand side of equation 3. The entries in $\mathbf{M}$ depend on the grid spacing and the frequency-dependent medium properties; $\mathbf{M}$ is sparse with up to 13 nonzero entries per line.

At the model edges, Dirichlet and Neumann boundary conditions have been tested, assuming that either the electric field values or the derivatives of the tangential fields are zero at the boundaries. Both assumptions are crude and require that the boundaries be located sufficiently far from the sources. To mitigate boundary artifacts, cell sizes are permitted to grow toward the boundaries. I use Dirichlet boundaries for the tests in this paper because, in contrast to Neumann boundaries, they allow making the system matrix symmetric by applying simple scaling factors to the components of the discretized Helmholtz equation (Newman and Alumbaugh, 1995; see Appendix A). This increases the efficiency of solving equation system 8 by nearly a factor of two and also increases the maximum feasible model size.

The chosen staggering scheme, with the electric-field components located on the cell faces and the magnetic-field components on the edges, is used by Haber et al. (2000) and Haber and Ascher (2001). When modeling CSEM surveys, this scheme is advantageous over the (more commonly used) scheme with the electric-field components on the edges and magnetic-field components on the faces. This is because of the positions of secondary-source points relative to the physical source, as illustrated in Figure 2. For a horizontal-dipole source, the strongest secondary sources, which have a dominant influence on the modeling errors, are present in the x-component J^S_x of the secondary-source field, at the locations nearest to the physical source. For the chosen scheme, the vertical position of J^S_x nodes is at the cell centers in the z-direction (Figure 2a).

For the opposite scheme with electric-field components on the edges, J^S_x nodes are located at cell boundaries in the vertical direction (Figure 2b). The distances between the physical source and the closest secondary-source points are shorter for the opposite scheme than for the scheme I use (thin dashed arrows, Figure 2) because the vertical medium averaging affects the x-component in the opposite scheme. This results in stronger field gradients in the source field J^S_x and, consequently, larger errors caused by spatial undersampling than for the scheme depicted in Figure 2a.

Matrix factorization and solution

Equation system 8 is solved using the MUMPS package (Amestoy et al., 2001, 2006). For symmetric matrices, MUMPS performs an LDL^T factorization, which is nearly twice as memory and time efficient as standard LU factorization of nonsymmetric matri-

ces (Amestoy et al., 2006). MUMPS uses a multifrontal approach (Duff and Reid, 1983; Amestoy et al., 2006) and is parallelized for distributed-memory architectures using the MPI standard. Elaborate multilevel parallelization and load-distribution strategies are crucial for making MUMPS efficient (Amestoy et al., 2001, 2006). In contrast to iterative approaches (e.g., Freund and Nachtigal, 1994), the direct solution permits, after completing the factorization for a single frequency, obtaining electric fields for multiple source points with little computational effort by repeatedly using the same factorization. Obviously, the efficiency of such an approach depends critically on the initial factorization cost and the number of source points.

To assess the computational requirements of the MUMPS solver for the task at hand, I conduct a series of tests (using MUMPS versions 4.8.3 and 4.8.4). The results are summarized in Figure 3. Computations, run on a small test cluster, use up to 12 processing cores with 48 GB total available memory. In contrast to Operto et al. (2007), who use real-valued single-precision arithmetic in their assessment of the MUMPS solver for 3D seismic modeling, I use complex double-precision arithmetic to obtain accurate EM modeling results. I test model sizes ranging from $9 \times 6 \times 5$ to $90 \times 44 \times 80$ cells. This corresponds to $N = 3N_xN_yN_z = 810$ to $950,400$ unknown electric-field values. Most of the tests were run three times to account for variations in system and network load (three of the large tests on 12 processors were run only twice).

As expected, memory demand increases rapidly with increasing model size (Figure 3a). The largest memory (~ 47 Gbytes) was required by the second-largest model. This apparent anomaly in memory use might be explained by the slightly different sparsity patterns of the two largest models that resulted from the $91 \times 86 \times 40$ and $90 \times 44 \times 80$ grids, respectively. The factorization for the most memory-intensive model required $\sim N^{1.518}$ LDL^T factors. Because of this, if larger models are to be computed, the size of the cluster must increase more than linearly with the desired model size. Some additional overhead is required if the number of processes increases because the required total memory for a given model also increases with the number of processes (Figure 3a).
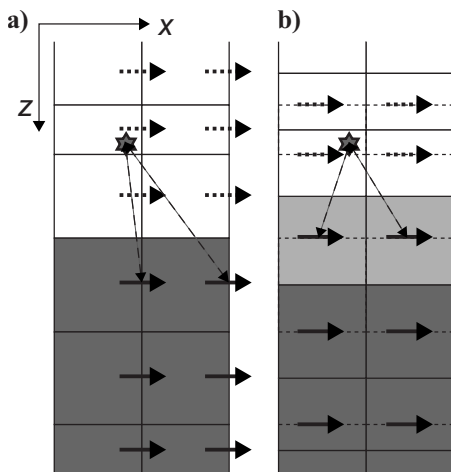
The matrix factorization (Figure 3b) took ~ 1.9 hours for the largest model tested. As expected, increasing the number of processes for a given model size reduces the computation time until speedup is counteracted by the increasing communication overhead. For the tested models, the number of floating-point operations required for the factorization was on the order of a multiplication factor (roughly seven) times N^2. The associated increase of the number of floating-point operations for increasing model size is expected to be only partly compensable by increasing the number of processes.

The times needed for the solution step generally amount to a small fraction of those required for the factorization (Figure 3c). For the six largest models, the solution for one source was roughly 500–950 times faster than the matrix factorization. Some speedup with increasing number of processes is observed, but the scaling behavior of the solution step is expectedly not as good as that of the factorization (Duff and Reid, 1983; Amestoy et al., 2006). Although the factorization times vary only slightly between test runs for any given model, there are relatively large fluctuations for the solution time, probably caused by variations in the network load.
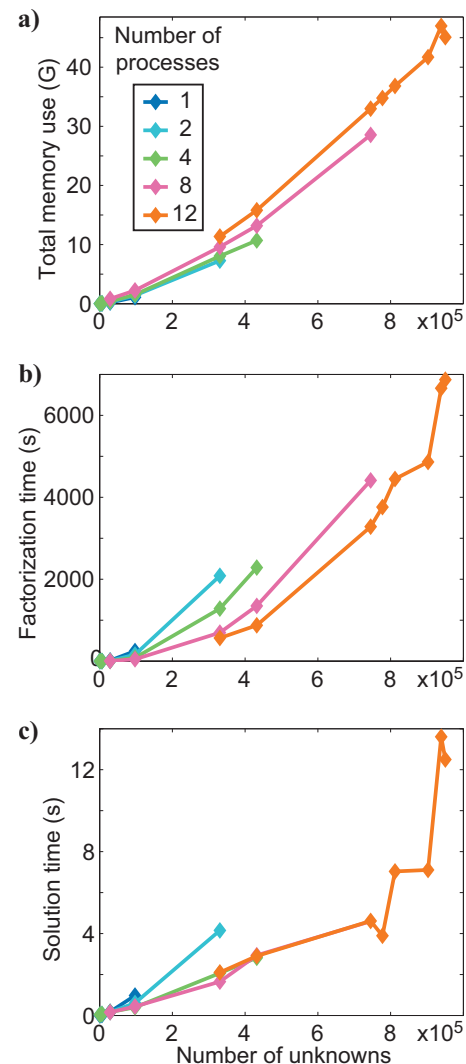

Figure 2. The (x,z) positions of secondary-source nodes J_x^S for the staggering schemes with electric fields (a) on the cell faces and (b) on the cell edges. Gray shading indicates conductivities different from the background conductivity. Conductivities are vertically averaged in (b). The stars denote physical sources; solid wide arrows denote secondary sources. Thin dashed arrows indicate the distances between the physical source and the nearest secondary sources. These distances are shorter in (b) than in (a).

Figure 3. Results of testing the performance of the MUMPS direct solver for 3D EM modeling for various model sizes. (a) Memory usage. (b) Time for LDL^T factorization. (c) Time for computing a single solution. The colors indicate different numbers of processes.

Field interpolation to receiver positions

CSEM receiver devices typically measure several EM-field components at the same position (Constable and Srnka, 2007). Accordingly, for realistic simulation of CSEM surveys, the fields computed at the staggered-grid locations must be interpolated to the given receiver positions. In doing so, we must account for possible discontinuities of the normal component of the electric field at any cell boundary at which the medium is discontinuous. Instead of interpolating the electric fields directly, the generalized current density **J** $= \sigma^* \mathbf{E}$ can be used here because **J** is continuous across model discontinuities (Haber et al., 2000). This first requires calculating the total field (i.e., the sum of the primary and secondary fields) and then interpolating the total-field values.

Unfortunately, total-field interpolation is inaccurate where the EM field is poorly approximated by a simple (e.g., linear) interpolation function. Errors caused by interpolating the total field are particularly severe near the source and can be substantial near model discontinuities where the fields vary rapidly. To improve interpolation accuracy, it is advantageous to use an interpolation based on the secondary fields only. I show the derivation of a continuous, secondary-field-based quantity using the example of the z-components J_z and E_z of the current density and the electric field (analogous considerations are valid for the x- and y-components).

The total current density J_z is

$$J_z = E_z \sigma_z^*, \tag{9}$$

where σ_z^* denotes z-staggered complex conductivity. Replacing the total electric field by the sum of the primary and secondary fields, we obtain

$$J_z = E_z^P \sigma_z^* + E_z^S \sigma_z^*. \tag{10}$$

Although the total current density on the left side of equation 10 is continuous, this does not hold for either of the terms on the right-hand side. However, the primary current density J_z^P,

$$J_z^P = E_z^P \sigma_z^{P*}, \tag{11}$$

is continuous. Inserting this into equation 10 results in

$$J_z = E_z^P \sigma_z^{P*} + [E_z^P(\sigma_z^* - \sigma_z^{P*}) + E_z^S \sigma_z^*]. \tag{12}$$

Because the left side and the first term on the right side of equation 12 are continuous, the term in brackets must be continuous as well. This term is used for interpolating the electric fields. Near the physical source, the total and background conductivities are equal, so the interpolation includes only the secondary current density $E_z^S \sigma_z^*$ and no contribution from the rapidly varying primary field. Where the total and background conductivities differ, the interpolation errors often can be reduced significantly by excluding the contribution of $E_z^P \sigma_z^{P*}$ from the interpolation.

To obtain field values at a given receiver location z_r, I first compute the quantity in brackets in equation 12, then interpolate this linearly to position z_r, recover the secondary field value E_z^S, using the primary field E_z^P computed explicitly at position z_r and the original nonaveraged total and background conductivities σ^* and σ^{P*}, and finally add E_z^S and E_z^P. This procedure accurately recovers fields near the ocean bottom, where receivers typically are placed in CSEM experiments.

Magnetic-field components on the staggered grid (see Figure 1) are computed by straightforward finite-difference evaluation of equation 2a. Because the magnetic permeability is assumed to be constant, all magnetic-field components are continuous throughout the model. Therefore, magnetic-field values at given receiver locations can be computed by interpolating the scattered magnetic-field components and then adding background field values evaluated directly at the receiver locations.

VERIFICATION OF THE MODELING SCHEME

The accuracy of the described modeling approach is verified by comparing the FDFD modeling results to results obtained from a reflectivity method capable of computing 3D fields for horizontally layered media (Løseth and Ursin, 2007). In this way, I demonstrate the influence of the background model, the staggering scheme, and the new interpolation technique. To allow a comprehensive view of modeling accuracy, vertical slices through model data volumes are shown, rather than the seafloor data typical of real CSEM surveys.

I conducted various tests using models A and B displayed in Figure 4. Both models contain a water layer with conductivity $\sigma = 3.6$ S/m and relative permittivity $\varepsilon_r = 80$, and a sediment unit with $\sigma = 0.5$ S/m and $\varepsilon_r = 8$, in which a 100-m-thick resistive layer with $\sigma = 0.02$ S/m and $\varepsilon_r = 4$ is embedded 1000 m below the seafloor. Model B includes an air layer ($\sigma = 0$, $\varepsilon_r = 1$) above the 300-m-deep water (Figure 4b).

In both models, the x and y spacing is constant at 80 m. The z spacing is variable to improve modeling accuracy, with d$z = 20$ m for the thinnest cells at the layer boundaries. Outside the range shown in Figure 4, both models are padded at each side with five cells whose size increases by a factor of two from one cell to the next. This minimizes boundary artifacts. The total number of cells is $N_x \times N_y \times N_z = 90 \times 60 \times 46 = 248,400$ for model A and $90 \times 60 \times 48 = 259,200$ for model B. A frequency of 1 Hz is used.

The relatively coarse grid spacing allows demonstrating error effects and facilitates assessing the accuracy for multisource modeling. To enable the repeated use of a once-factorized matrix for multiple sources, the system matrix and, accordingly, the model grid must be the same for all sources; specific grid adaptations such as using smaller cells near the source would require a new factorization for every new grid.

To assess the errors that can be expected for the chosen grid spacing, I relate the wavenumber content of the data, as obtained from 1D
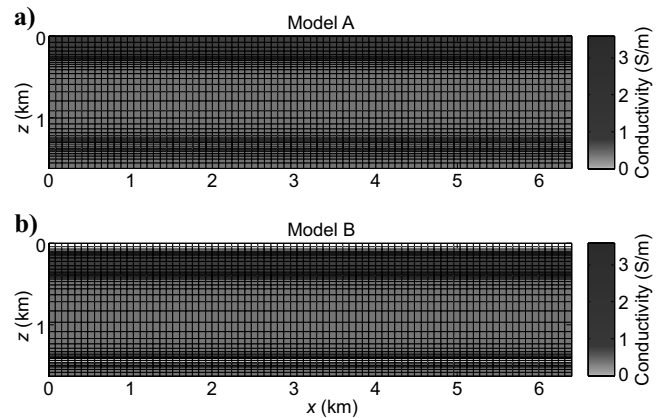

Figure 4. Conductivity models (a) without and (b) with an air layer used for testing the modeling approach. The x and y grid spacing is regular; the z grid spacing is variable. Conductivity and permittivity values are given in the main text.
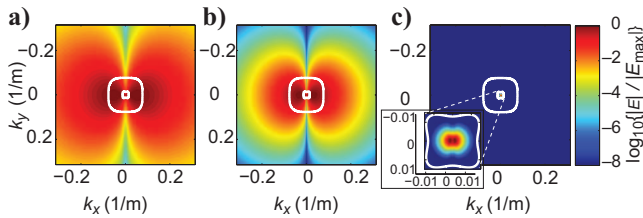
Figure 5. Wavenumber-domain electric fields E_x for model B (see Figure 4) 10 m above the seafloor, normalized to the maximum within each plot. (a) Total field. (b) Secondary field for a homogeneous background. (c) Secondary field for a 1D background that does not include the resistive layer. The white contours indicate 5% error estimates, obtained using the approximation from Smith (1996a), for cell sizes of $80 \times 80 \times 20$ m (inner lines) and $10 \times 10 \times 10$ m (outer lines).
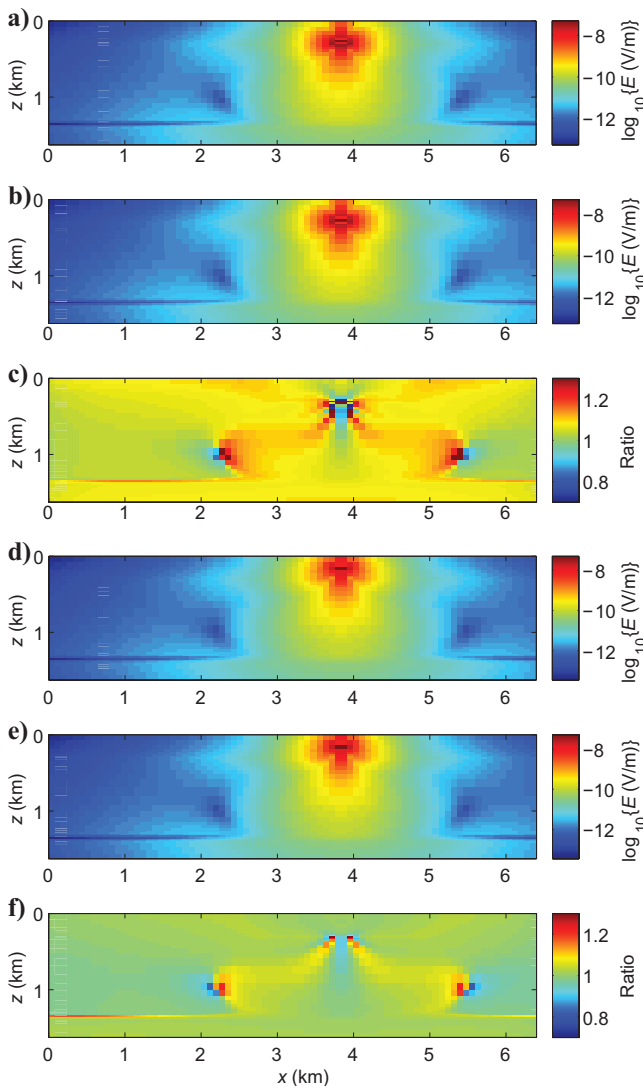

Figure 6. Vertical slices through electric-field E_x component data generated for model A (Figure 4a). The background model is homogeneous with water conductivity and permittivity. The source is located at (a–c) 30 m and (d–f) 150 m above the seafloor. (a, d) FDFD modeling results $|E_x^{\mathrm{FD}}|$. (b, e) Results from 1D reflectivity modeling $|E_x^{\mathrm{refl}}|$. (c, f) Ratios R between the FDFD and reflectivity data, computed as $R = |E_x^{\mathrm{FD}}/E_x^{\mathrm{refl}}|$.

modeling, to wavenumber-based error estimates given by Smith (1996a). Figure 5 shows E_x data in the horizontal wavenumber domain, 10 m above the seafloor and 20 m below the source. Following Smith (1996a), I estimate the expected discretization-related errors by taking the relative difference between the discrete and continuous vertical wavenumbers k_z for a given cell size and given horizontal wavenumbers. The white contours near the centers of the plots in Figure 5 mark the wavenumbers (k_x, k_y) at which a 5% error in k_z is expected for a cell size of $80 \times 80 \times 20$ m. For comparison, the outer contours indicate a 5% error level for $10 \times 10 \times 10$-m cells.

For the total field and secondary field with a homogeneous background (Figure 5a and b), most of the wavefield at this depth is located outside the inner contour, indicating that large errors must be expected. The error estimate might be somewhat pessimistic (Smith, 1996a), and high-wavenumber components decay rapidly with increasing distance from the source. Nevertheless, this analysis suggests that $80 \times 80 \times 20$-m cells are too large for accurate modeling with a homogeneous background. In contrast, the secondary field obtained when using a 1D background reaches insignificant levels at very low wavenumbers (see inset, Figure 5c), suggesting that the chosen cell size is sufficient to obtain accurate 3D modeling results here. Note that the outlined analysis provides only a rough indication of expected error levels; for more thorough investigations, vertical and lateral model inhomogeneity should be taken into account.

Influence of the background model

Figure 6 shows examples of E_x component data generated for model A (see Figure 4a). A horizontal x-directed electric-dipole source is located 30 m (Figure 6a-c) and 150 m (Figure 6d-f) above the seafloor. The background is a homogeneous model having the water conductivity and permittivity. Receivers are placed in the cell centers throughout a vertical section through the model. FDFD modeling results are shown in Figure 6a and d, and 1D reflectivity modeling results are shown for reference in Figure 6b and e. Figure 6c and f shows the ratios between the FDFD and reflectivity modeling results, computed by first taking the ratio and then the absolute value, so that both amplitude and phase are included in the comparison.

For the source located 30 m above the seafloor, a relatively high accuracy is achieved in spite of the pessimistic error estimate (Figure 5b). This might be because of the source position at a cell center; generally, the best accuracy has been observed for source positions symmetric to the grid (Weiss and Constable, 2006). Nevertheless, in the lowest-amplitude regions and near the source, the FDFD results deviate from the reflectivity results by up to 30%. Errors of this magnitude are nearly on the order of expected anomalies from hydrocarbon reservoirs (Srnka et al., 2006) and therefore are unacceptable. Likely, the errors are caused primarily by insufficient sampling of the secondary-source field (see right-side of equation 3) immediately beneath the seafloor. Strong gradients occur in the source field only 30 m from the source, and the x and y spacing of 80 m is too coarse to adequately sample the associated high wavenumbers present in the source field. The accuracy is significantly higher for the source located 150 m above the seafloor (Figure 6d-f), with errors mostly less than 10%. Here, gradients in the secondary-source field are weaker.

In Figure 7, data are shown for model A, with the source located 30 m above the seafloor and with a 1D layered background model. The background includes the water and conductive sediment but not the 100-m-thick resistive layer. Using a 1D layered background de-

creases the error level significantly. Errors near the source practically disappear, and the errors in the regions of lowest amplitudes at horizontal distances of ~2.2 and 5.4 km decrease to about 5% (note the different color bars in Figures 6c and 7b). Small residual errors near the model boundaries are probably primarily caused by boundary effects.

A closer approximation of real survey conditions is achieved by models that include air (Constable and Srnka, 2007). Figure 8 shows E_x data computed for model B, which contains an air layer (see Figure 4b). This test shows that for a model containing air, accurate results are obtained only if a 1D layered background model is used. For the 1D background (Figure 8c and d), the errors in all layers are only slightly larger than those occurring for the model without air (compare Figures 7b and 8d). In contrast, for a homogeneous background (Figure 8a and b), reliable field values cannot be obtained.

It is noteworthy that the system matrix **M** is identical for the homogeneous and 1D background fields; the only difference is in the secondary-source vector $\mathbf{J}^s$ (i.e., the right side of equation 8). This indicates that the major material contrast of the air-water interface is accounted for correctly and numerically accurately in the matrix factorization; using the true air properties is possible and does not result in numerical singularities in the system of equation 8. (Nevertheless, air can be modeled by using an artificial small conductivity; tests show that this results in changes of the electric-field values at the seafloor well below the error level of the simulations.)

Influence of the staggering scheme

Figure 9 shows electric-field data computed using a staggering scheme in which the electric-field components are located on the cell edges and the magnetic-field components are on the faces (i.e., a scheme opposite to that displayed in Figure 1 and used for all other tests). For model A and a homogeneous background with a horizontal-dipole source located near the seafloor, the errors resulting from this staggering scheme are significantly larger than those resulting from the scheme with the electric-field components on the faces. The median error throughout the slice displayed in Figure 9a is 14.3%, whereas the median error for the slice displayed in Figure 6a is only 7.1%. A similar, although weaker, effect is also observed when using a 1D background model. For electric fields located on the cell faces, the median error throughout the slice shown in Figure 7 is 0.23%,
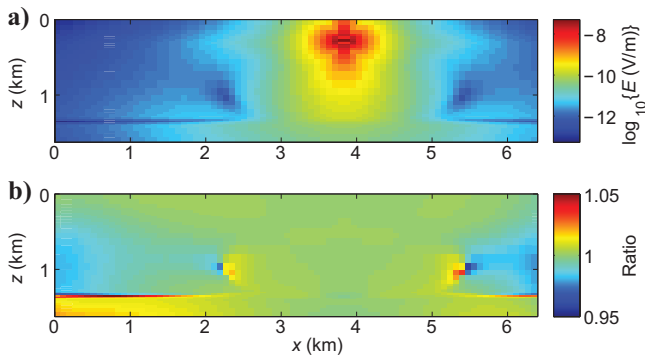
whereas the median error is 0.36% when computing the same data using the opposite staggering scheme. These results confirm that the chosen staggering scheme is advantageous for simulating typical CSEM surveys.

Interpolation

The effect of the new interpolation scheme is best shown using the E_z component because E_z contains major discontinuities for the 1D test models. In Figure 10, I compare data obtained from shifting the total fields (Figure 10a and b) and shifting the quantity in brackets in
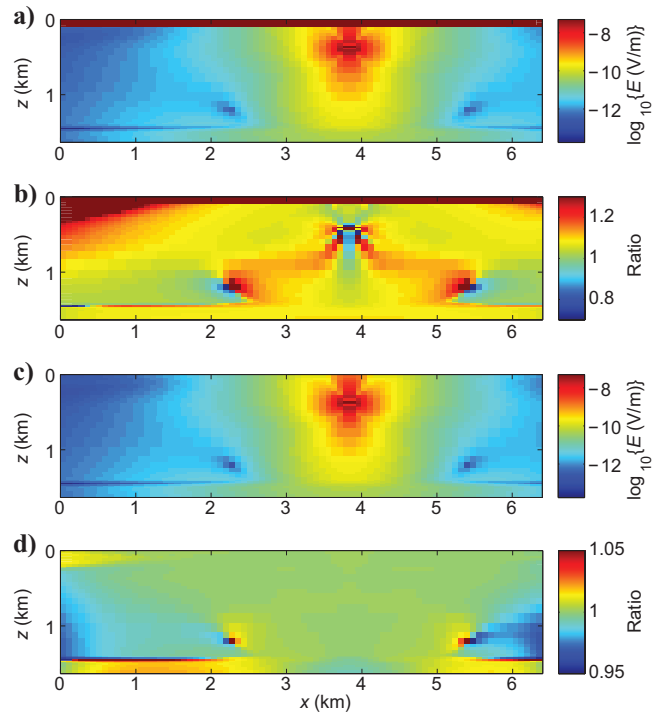
Figure 8. Vertical slices through E_x data generated for model B (Figure 4b). The background model is (a, b) a homogeneous model having water conductivity and permittivity and (c, d) a 1D layered model that includes the air, water, and conductive sediment but not the resistive layer. The source is located 30 m above the seafloor. (a, c) FDFD modeling results. (b, d) Ratios between the FDFD and reference reflectivity data. Note the different color bars in (b) and (d).

Figure 7. Vertical slices through E_x data generated for model A (Figure 4a). The background model is a 1D layered model that does not include the resistive layer. The source is located 30 m above the seafloor. (a) FDFD modeling results. (b) Ratio between FDFD data and reference reflectivity data displayed in Figure 6b. Note the different color bars in (b) and Figure 6c.
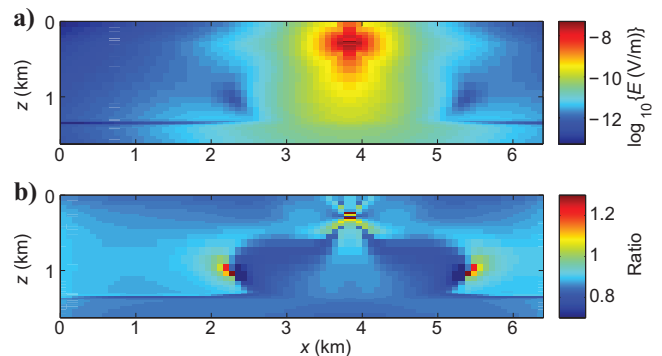
Figure 9. The same as Figure 6a and c, but computed using a staggering scheme in which the electric-field components are located on the cell edges and the magnetic-field components on the faces, opposite to the scheme displayed in Figure 1.
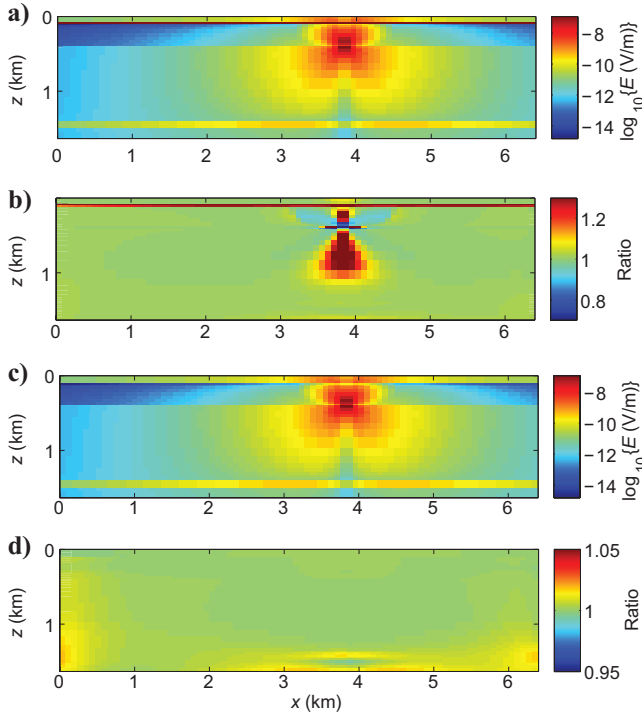
Figure 10. Vertical slices through electric-field E_z component data generated for model B (Figure 4b). The data were interpolated to receiver locations in the cell centers using (a, b) the total current densities and (c, d) the quantity in brackets in equation 12. The background model is a 1D layered model that does not include the resistive layer, and the source is located 30 m above the seafloor. (a, c) FDFD modeling results. (b, d) Ratios between FDFD and reference reflectivity data. Note the different color scales in (b) and (d).
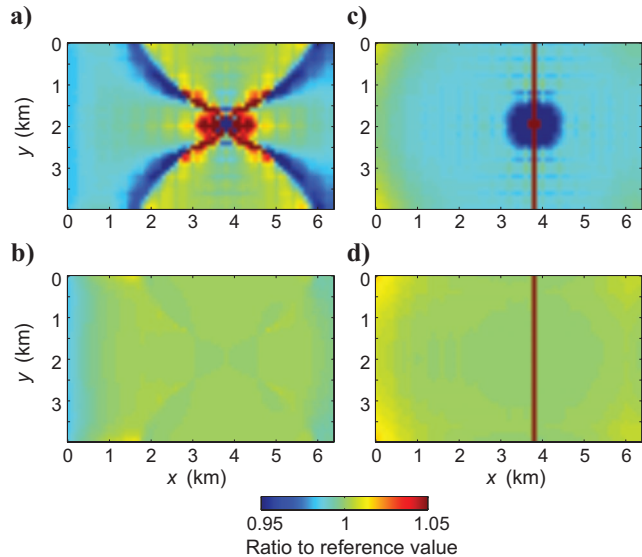

Figure 11. Errors of the (a, b) E_x and (c, d) E_z component for model B (Figure 4b) and receivers located 1 m above the seafloor. The ratios $R = \left| E_{\{x,z\}}^{FD} / E_{\{x,z\}}^{refl} \right|$ are shown. In (a) and (c), results from interpolating total fields to the receiver locations are displayed. In (b) and (d), results from interpolating the term in brackets in equation 12 are displayed.

equation 12 (Figure 10c and d). By using the new shifting method, the overall accuracy improves significantly, and interpolation artifacts across the layer boundaries disappear. Remarkably, the new interpolation scheme even recovers accurately the fields across the airwater interface. Strong artifacts near the source, which result from the poor approximation of the total fields by the simple linear interpolation function, also are eliminated.

In Figure 10, the points closest to the seafloor are located 10 m above the seafloor. In Figure 11, the electric-field errors relative to reference data computed using the reflectivity method are displayed for receivers located 1 m above the seafloor. This corresponds more closely to real CSEM survey conditions. For the E_x component, which is continuous across the seafloor, and the E_z component, which is discontinuous, the new interpolation technique produces significantly more accurate results than interpolation of the total fields. For 3D models that contain discontinuities in the x- and y-directions, the same improvement of accuracy can be expected for interpolations in the x- and y-directions.

THREE-DIMENSIONAL EXAMPLE

To verify my modeling scheme for 3D models, I use the canonical disc model from Constable and Weiss (2006). This model contains a circular 100-m-thick resistive disc embedded in conductive sediment 1 km below the seafloor (Figure 12). Disc diameters of 2 and 5 km were tested. A unit-amplitude, 1-Hz, x-directed dipole source was located above the left edge of the discs, 100 m above the seafloor. I discretized the models using variable cell sizes in all directions, with a minimum x and y spacing of 50 m and a minimum z spacing of 25 m. The grids contained $99 \times 76 \times 40$ cells for the 2 -km disc and $91 \times 86 \times 40$ cells for the 5-km disc.

Simulated data for the E_x and E_z components were extracted along an x-line beneath the source, 0.1 mm above the seafloor (Figure 13). The E_x amplitudes and phases (Figure 13a and b) produced by the modeling scheme show excellent agreement with data from Constable and Weiss (2006). Slight phase differences at offsets greater than 7 km for the 2-km disc probably are caused by the somewhat too coarse discretization near the model edge. For the E_z component, the shape of the curves agrees very well, but I obtain lower amplitudes than Constable and Weiss (2006) when extracting data 0.1 mm above the seafloor and higher amplitudes when extracting data 0.1 mm below (Figure 13c). Here, the values from Constable and Weiss (2006) likely represent an average of E_z across the seafloor discontinuity. In contrast, my interpolation scheme correctly recovers the fields immediately above and below the seafloor.
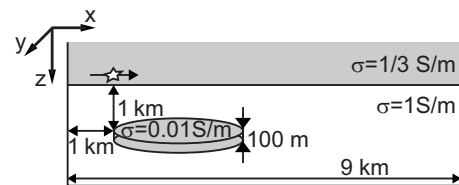

Figure 12. The 3D disc model from Constable and Weiss (2006) used for verifying the modeling scheme (not to scale).
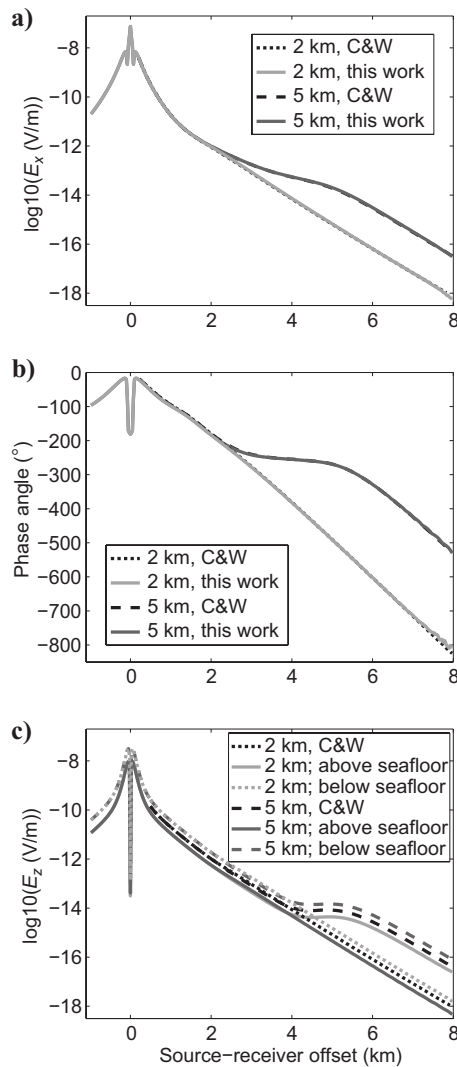
Figure 13. Comparison of data obtained from the new modeling scheme to data presented by Constable and Weiss (2006) for the model shown in Figure 12 with disc diameters of 2 and 5 km. Displayed are (a) E_x amplitudes, (b) E_x phases, and (c) E_z amplitudes. I extracted data in the source plane, 0.1 mm above the seafloor. In (c), data extracted 0.1 mm below the seafloor are also shown. C&W = Constable and Weiss (2006).

CONCLUSIONS

A new modeling scheme allows accurate simulation of CSEM surveys with sources and receivers located near the seafloor. Careful implementation at sufficient numerical precision is vital to accommodate major material contrasts such as between air and the subsurface. The specific optimizations described are well suited for simulating CSEM surveys. The chosen staggering scheme with the electric-field components on the cell faces and the magnetic-field components on the edges improves modeling accuracy for horizontal-dipole sources near the seafloor. A new interpolation technique extracts electric-field values at given receiver positions. It uses the generalized current density of the secondary field, supplemented by a secondary-source term to ensure that a continuous quantity is interpolated. For the test models considered, this new interpolation is more accurate than interpolation of the total current densities and

provides highly accurate field values even in the immediate vicinity of the major model discontinuity posed by the seafloor.

The accuracy achieved by the modeling scheme, with field values being precise within 5% or less down to the lowest amplitudes that occurred for the tested models, makes the scheme suitable for applications within hydrocarbon exploration. However, to enhance the usefulness for such applications, models larger than those shown here need to be used because many CSEM surveys contain maximum offsets of 20 km or more. Unfortunately, the memory demand of the direct solver grows with model size at an exponential rate significantly larger than one, so a moderate increase in model size requires a considerable growth of the cluster on which the code is run. Larger model sizes can be handled for the widely used 0.25-Hz frequency by increasing cell sizes. At and above the 1-Hz frequency used here, use of this scheme on present-day industry-size clusters is conceivable, but alternative (i.e., iterative) solution techniques are probably more economical for large-scale models.

To facilitate reusing a single-matrix factorization for multiple sources, a constant grid must be used for all sources considered, and grid refinement near the source is not permissible. In this situation, a 1D background model is important to achieve satisfactory accuracy for the rather coarse model discretization required to obtain reasonable model sizes. Using a 1D background substantially reduces the high-wavenumber content of the secondary fields and permits accurate simulations for models that include air. In contrast, for homogeneous backgrounds, secondary sources occurring immediately beneath the seafloor (and in air, if present in the model) result in high-wavenumber components in the secondary fields, so that dense sampling is required and poor data are produced for models containing air.

Unfortunately, accurate calculations of 1D background fields using the adaptive integration technique are computationally expensive. This counteracts benefits gained from the direct-solution approach. The efficiency of the 1D background computations might be improved significantly by using, at least for parts of the computations, fast Hankel transforms instead of explicit adaptive integral evaluation.

The verifications on 1D and 3D models indicate that this modeling scheme can produce reasonable 3D modeling results. Future tests should include other models containing various 3D structures, such as reservoir geometries and nonflat bathymetry. For such models, additional difficulties probably will arise because of the blocky discretization, with staircase effects being a well-known problem of finite-difference methods. Various extensions of the scheme are conceivable (e.g., including anisotropy), and I anticipate that this scheme will form a suitable basis for an inversion algorithm.

APPENDIX A

FINITE-DIFFERENCE EQUATIONS

The Helmholtz equation 3 is discretized as in Newman and Alumbaugh (1995), but using the staggering scheme displayed in Figure 1. The resulting discrete finite-difference equations are

$$
\frac{1}{\Delta y_j}\left[\frac{E^{yS}_{i+1,j+\frac{1}{2},k} - E^{yS}_{i,j+\frac{1}{2},k}}{\Delta x_{i+\frac{1}{2}}} - \frac{E^{yS}_{i+1,j-\frac{1}{2},k} - E^{yS}_{i,j-\frac{1}{2},k}}{\Delta x_{i+\frac{1}{2}}}\right]
$$

$$
- \frac{1}{\Delta y_j}\left[\frac{E^{xS}_{i+\frac{1}{2},j+1,k} - E^{xS}_{i+\frac{1}{2},j,k}}{\Delta y_{j+\frac{1}{2}}}\right.
$$

$$
\left. - \frac{E^{xS}_{i+\frac{1}{2},j,k} - E^{xS}_{i+\frac{1}{2},j-1,k}}{\Delta y_{j-\frac{1}{2}}}\right]
$$

$$
+ \frac{1}{\Delta z_k}\left[\frac{E^{zS}_{i+1,j,k+\frac{1}{2}} - E^{zS}_{i,j,k+\frac{1}{2}}}{\Delta x_{i+\frac{1}{2}}}\right.
$$

$$
\left. - \frac{E^{zS}_{i+1,j,k-\frac{1}{2}} - E^{zS}_{i,j,k-\frac{1}{2}}}{\Delta x_{i+\frac{1}{2}}}\right]
$$

$$
- \frac{1}{\Delta z_k}\left[\frac{E^{xS}_{i+\frac{1}{2},j,k+1} - E^{xS}_{i+\frac{1}{2},j,k}}{\Delta z_{k+\frac{1}{2}}}\right.
$$

$$
\left. - \frac{E^{xS}_{i+\frac{1}{2},j,k} - E^{xS}_{i+\frac{1}{2},j,k-1}}{\Delta z_{k-\frac{1}{2}}}\right] + j\omega\mu_0\sigma^*_{i+\frac{1}{2},j,k}E^{xS}_{i+\frac{1}{2},j,k}
$$

$$
= -j\omega\mu_0\left(\sigma^*_{i+\frac{1}{2},j,k} - \sigma^{P*}_{i+\frac{1}{2},j,k}\right)E^{xP}_{i+\frac{1}{2},j,k}, \qquad \text{(A-1)}
$$

$$
\frac{1}{\Delta z_k}\left[\frac{E^{zS}_{i,j+1,k+\frac{1}{2}} - E^{zS}_{i,j,k+\frac{1}{2}}}{\Delta y_{j+\frac{1}{2}}} - \frac{E^{zS}_{i,j+1,k-\frac{1}{2}} - E^{zS}_{i,j,k-\frac{1}{2}}}{\Delta y_{j+\frac{1}{2}}}\right]
$$

$$
- \frac{1}{\Delta z_k}\left[\frac{E^{yS}_{i,j+\frac{1}{2},k+1} - E^{yS}_{i,j+\frac{1}{2},k}}{\Delta z_{k+\frac{1}{2}}}\right.
$$

$$
\left. - \frac{E^{yS}_{i,j+\frac{1}{2},k} - E^{yS}_{i,j+\frac{1}{2},k-1}}{\Delta z_{k-\frac{1}{2}}}\right]
$$

$$
+ \frac{1}{\Delta x_i}\left[\frac{E^{xS}_{i+\frac{1}{2},j+1,k} - E^{xS}_{i+\frac{1}{2},j,k}}{\Delta y_{j+\frac{1}{2}}}\right.
$$

$$
\left. - \frac{E^{xS}_{i-\frac{1}{2},j+1,k} - E^{xS}_{i-\frac{1}{2},j,k}}{\Delta y_{j+\frac{1}{2}}}\right]
$$

$$
- \frac{1}{\Delta x_i}\left[\frac{E^{yS}_{i+1,j+\frac{1}{2},k} - E^{yS}_{i,j+\frac{1}{2},k}}{\Delta x_{i+\frac{1}{2}}}\right.
$$

$$
\left. - \frac{E^{yS}_{i,j+\frac{1}{2},k} - E^{yS}_{i-1,j+\frac{1}{2},k}}{\Delta x_{i-\frac{1}{2}}}\right] + j\omega\mu_0\sigma^*_{i,j+\frac{1}{2},k}E^{yS}_{i,j+\frac{1}{2},k}
$$

$$
= -j\omega\mu_0\left(\sigma^*_{i,j+\frac{1}{2},k} - \sigma^{P*}_{i,j+\frac{1}{2},k}\right)E^{yP}_{i,j+\frac{1}{2},k}, \qquad \text{(A-2)}
$$

$$
\frac{1}{\Delta x_i}\left[\frac{E^{xS}_{i+\frac{1}{2},j,k+1} - E^{xS}_{i+\frac{1}{2},j,k}}{\Delta z_{k+\frac{1}{2}}} - \frac{E^{xS}_{i-\frac{1}{2},j,k+1} - E^{xS}_{i-\frac{1}{2},j,k}}{\Delta z_{k+\frac{1}{2}}}\right]
$$

$$
- \frac{1}{\Delta x_i}\left[\frac{E^{zS}_{i+1,j,k+\frac{1}{2}} - E^{zS}_{i,j,k+\frac{1}{2}}}{\Delta x_{i+\frac{1}{2}}}\right.
$$

$$
\left. - \frac{E^{zS}_{i,j,k+\frac{1}{2}} - E^{zS}_{i-1,j,k+\frac{1}{2}}}{\Delta x_{i-\frac{1}{2}}}\right]
$$

$$
+ \frac{1}{\Delta y_j}\left[\frac{E^{yS}_{i,j+\frac{1}{2},k+1} - E^{yS}_{i,j+\frac{1}{2},k}}{\Delta z_{k+\frac{1}{2}}}\right.
$$

$$
\left. - \frac{E^{yS}_{i,j-\frac{1}{2},k+1} - E^{yS}_{i,j-\frac{1}{2},k}}{\Delta z_{k+\frac{1}{2}}}\right]
$$

$$
- \frac{1}{\Delta y_j}\left[\frac{E^{zS}_{i,j+1,k+\frac{1}{2}} - E^{zS}_{i,j,k+\frac{1}{2}}}{\Delta y_{j+\frac{1}{2}}}\right.
$$

$$
\left. - \frac{E^{zS}_{i,j,k+\frac{1}{2}} - E^{zS}_{i,j-1,k+\frac{1}{2}}}{\Delta y_{j-\frac{1}{2}}}\right] + j\omega\mu_0\sigma^*_{i,j,k+\frac{1}{2}}E^{zS}_{i,j,k+\frac{1}{2}}
$$

$$
= -j\omega\mu_0\left(\sigma^*_{i,j,k+\frac{1}{2}} - \sigma^{P*}_{i,j,k+\frac{1}{2}}\right)E^{zP}_{i,j,k+\frac{1}{2}}. \qquad \text{(A-3)}
$$

Superscripts S and P denote the secondary and primary fields, respectively; Δx_i, Δy_j, and Δz_k are the widths of the main grid cells i, j, and k; and $\Delta x_{i+\frac{1}{2}}$, $\Delta y_{j+\frac{1}{2}}$, and $\Delta z_{k+\frac{1}{2}}$ are the distances between the centers of cells $i + 1$ and i, $j + 1$ and j, and $k + 1$ and k, respectively.

A symmetric system matrix, equal to that resulting from a finite-volume approach (Weiss and Constable, 2006), is obtained by multiplying equation A-1 by $\Delta x_{i+\frac{1}{2}}\Delta y_j\Delta z_k$, equation A-2 by $\Delta x_i\Delta y_{j+(1/2)}\Delta z_k$, and equation A-3 by $\Delta x_i\Delta y_j\Delta z_{k+\frac{1}{2}}$.

REFERENCES

Afanasjew, M., M. Eiermann, O. G. Ernst, and S. Güttel, 2008, Implementation of a restarted Krylov subspace method for the evaluation of matrix functions: Linear Algebra and Its Applications, **429**, 2293–2314.

Alumbaugh, D. L., G. A. Newman, L. Prevost, and J. N. Shadid, 1996, Three-dimensional wideband electromagnetic modeling on massively parallel computers: Radio Science, **43**, 1–23.

Amestoy, P. R., I. S. Duff, J.-Y. L'Excellent, and J. Koster, 2001, A fully asyn-

chronous multifrontal solver using distributed dynamic scheduling: SIAM Journal on Matrix Analysis and Applications, **23**, 15–41.

Amestoy, P. R., A. Guermouche, J.-Y. L'Excellent, and S. Pralet, 2006, Hybrid scheduling for the parallel solution of linear systems: Parallel Computing, **32**, 136–156.

Avdeev, D. B., 2005, Three-dimensional electromagnetic modelling and inversion from theory to application: Surveys in Geophysics, **26**, 767–799.

Avdeev, D. B., A. V. Kuvshinov, O. V. Pankratov, and G. A. Newman, 2002, Three-dimensional induction logging problems, Part I — An integral equation solution and model comparisons: Geophysics, **67**, 413–426.

Badea, E. A., M. E. Everett, G. A. Newman, and O. Biro, 2001, Finite-element analysis of controlled-source electromagnetic induction using Coulomb-gauged potentials: Geophysics, **66**, 786–799.

Blome, M., H. R. Maurer, and K. Schmidt, 2009, Advances in three-dimensional geoelectric forward solver techniques: Geophysical Journal International, **176**, 740–752.

Börner, R.-U., O. Ernst, and K. Spitzer, 2008, Fast 3-D simulation of transient electromagnetic fields by model reduction in the frequency domain using Krylov subspace projection: Geophysical Journal International, **173**, 766–780.

Champagne II, N. J., J. G. Berryman, and H. M. Buettner, 2001, FDFD: A 3D finite-difference frequency-domain code for electromagnetic induction tomography: Journal of Computational Physics, **170**, 830–848.

Chave, A. D., 1983, Numerical integration of related Hankel transforms by quadrature and continued fraction expansion: Geophysics, **48**, 1671–1686.

Commer, M., and G. Newman, 2004, A parallel finite-difference approach for 3D transient electromagnetic modeling with galvanic sources: Geophysics, **69**, 1192–1202.

Constable, S., and L. J. Srnka, 2007, An introduction to marine controlled-source electromagnetic methods for hydrocarbon exploration: Geophysics, **72**, no. 2, WA3–WA12.

Constable, S., and C. J. Weiss, 2006, Mapping thin resistors and hydrocarbons with EM methods: Insights from 1D modeling: Geophysics, **71**, no. 2, G43–G51.

de Hoop, A. T., 1995, Handbook of radiation and scattering of waves: Academic Press Inc.

Duff, I. S., and J. K. Reid, 1983, The multifrontal solution of indefinite sparse symmetric linear equations: ACM Transactions on Mathematical Software, **9**, 302–325.

Freund, R. W., and N. M. Nachtigal, 1994, An implementation of the QMR method based on coupled two-term recurrences: SIAM Journal on Scientific Computing, **15**, 313–337.

Haber, E., and U. M. Ascher, 2001, Fast finite volume simulation of 3D electromagnetic problems with highly discontinuous coefficients: SIAM Journal of Scientific Computing, **22**, 1943–1961.

Haber, E., U. M. Ascher, D. A. Aruliah, and D. W. Oldenburg, 2000, Fast simulation of 3D electromagnetic problems using potentials: Journal of Computational Physics, **163**, 150–171.

Hart, J. F., E. W. Cheney, C. L. Lawson, H. J. Maehly, C. K. Mesztenyi, J. R. Rice, H. G. Thatcher, Jr., and C. Witzgall, 1968, Computer approximations: John Wiley & Sons, Inc.

Johansen, S. E., H. E. F. Amundsen, T. Røsten, S. Ellingsrud, T. Eidesmo, and A. H. Bhuyian, 2005, Subsurface hydrocarbons detected by electromagnetic sounding: First Break, **23**, 31–36.

Løseth, L. O., and B. Ursin, 2007, Electromagnetic fields in planarly layered anisotropic media: Geophysical Journal International, **170**, 44–80.

Maaø, F. A., 2007, Fast finite-difference time-domain modeling for marine-subsurface electromagnetic problems: Geophysics, **72**, no. 2, A19–A23.

Mackie, R. L., T. R. Madden, and P. E. Wannamaker, 1993, Three-dimensional magnetotelluric modeling using difference equations — Theory and comparisons to integral equation solutions: Geophysics, **58**, 215–226.

Mitsuhata, Y., and T. Uchida, 2004, 3D magnetotelluric modeling using the T-Ω finite-element method: Geophysics, **69**, 108–119.

Newman, G. A., and D. L. Alumbaugh, 1995, Frequency-domain modelling of airborne electromagnetic responses using staggered finite differences: Geophysical Prospecting, **43**, 1021–1041.

Oldenburg, D. W., E. Haber, and R. Shekhtman, 2007, Rapid forward modeling of multi-source TEM data: Proceedings of the 4th International Symposium on Three-Dimensional Electromagnetics, 35–38.

——, 2008, Forward modeling and inversion of multi-source TEM data: 78th Annual International Meeting, SEG, Expanded Abstracts, 559–563.

Operto, S., J. Virieux, P. Amestoy, J.-Y. L'Excellent, L. Giraud, and H. B. H. Ali, 2007, 3D finite-difference frequency-domain modeling of visco-acoustic wave propagation using a massively parallel direct solver: A feasibility study: Geophysics, **72**, no. 5, SM195–SM211.

Ravaut, C., S. Operto, L. Improta, J. Virieux, A. Herrero, and P. Dell' Aversana, 2004, Multiscale imaging of complex structures from multifold wide-aperture seismic data by frequency-domain full-waveform tomography: Application to a thrust belt: Geophysical Journal International, **159**, 1032–1056.

Schenk, O., and K. Gärtner, 2004, Solving unsymmetric sparse systems of linear equations with PARDISO: Future Generation Computer Systems, **20**, 475–487.

——, 2006, On fast factorization pivoting methods for sparse symmetric indefinite systems: Electronic Transactions on Numerical Analysis, **23**, 158–179.

Schwarzbach, C., and K. Spitzer, 2006, Numerical simulation of electromagnetic wave propagation using vector finite elements: Proceedings of the 11th International Conference on Ground-Penetrating Radar, SIM.11.

Smith, J. T., 1996a, Conservative modeling of 3-D electromagnetic fields, Part I: Properties and error analysis: Geophysics, **61**, 1308–1318.

——, 1996b, Conservative modeling of 3-D electromagnetic fields, Part II: Biconjugate gradient solution and an accelerator: Geophysics, **61**, 1319–1324.

Srnka, L. J., J. J. Carazzone, M. S. Ephron, and E. A. Eriksen, 2006, Remote reservoir resistivity mapping: The Leading Edge, **25**, 972–975.

Ursin, B., 1983, Review of elastic and electromagnetic wave propagation in horizontally layered media: Geophysics, **48**, 1063–1081.

van der Kruk, J., 2001, Three-dimensional imaging of multi-component ground penetrating radar data: Ph.D. dissertation, Delft University of Technology.

van der Kruk, J., C. P. A. Wapenaar, J. T. Fokkema, and P. M. van den Berg, 2003, Three-dimensional imaging of multicomponent ground-penetrating radar data: Geophysics, **68**, 1241–1254.

Wannamaker, P. E., 1991, Advances in three-dimensional magnetotelluric modeling using integral equations: Geophysics, **56**, 1716–1728.

Weiss, C. J., and S. Constable, 2006, Mapping thin resistors and hydrocarbons with marine EM methods, Part II — Modeling and analysis in 3D: Geophysics, **71**, no. 6, G321–G332.

Weiss, C. J., and G. A. Newman, 2002, Electromagnetic induction in a fully 3D anisotropic earth: Geophysics, **67**, 1104–1114.

Woźniakowski, H., 1980, Roundoff-error analysis of a new class of conjugate-gradient algorithms: Linear Algebra and Its Applications, **29**, 507–529.